Contents lists available at ScienceDirect

# Colloids and Surfaces B: Biointerfaces

# Microgel dynamics within the 3D porous structure of transparent PEG hydrogels

Gavino Bassu [1,2], Marco Laurati [1,3], Emiliano Fratini [*,4]

*Department of Chemistry "Ugo Schiff" and CSGI, University of Florence, via della Lastruccia, 3 – Sesto Fiorentino, FI I-50019, Italy*

ABSTRACT

We report an investigation on the effects of the confinement imposed by application-relevant poly(ethylene glycol) (PEG) hydrogel matrices with controlled porosity on the dynamics of soft microgels. Through a detailed characterization of the internal structure of the hydrogels at the nano and microscale, we were able to link the microgel dynamics, measured by particle tracking, to the 3D geometrical confinement imposed by the porous matrices. PEG hydrogels with a high degree of transparency and tunable pore sizes and volume fractions were obtained using freeze-thawing. We found that the porosity of the hydrogel networks is characterized by elongated channels having asymmetric sections, with the average size decreasing from about 7 to about 2 particle diameters, and the size distribution becoming narrower with increasing PEG content in the pre-reaction mixture. The microgel dynamics slowdown and change from diffusive to sub-diffusive as a result of the increasing confinement. The observed decrease in diffusivity is consistent with models of diffusion in cylindrical pores and can be attributed to hydrodynamic and steric effects in addition to geometrical constriction. A dependence of the effective diffusion coefficient on the pore volume fraction, which is unusually pronounced, suggests the presence of microgel-hydrogel interactions. Our results demonstrate that a detailed characterization of the 3D geometry of the porous network is of primary importance for the understanding of transport properties in complex, random porous media.

## 1. Introduction

Many interesting phenomena in physics and biology, and applications in materials science, medicine, environmental science and geology, are associated with the diffusion of nanometric and micrometric colloidal particles in three-dimensional confining matrices[1]. For example micro-filtration using porous matrices is needed to preserve vehicles or instruments from unwanted particulates[1] or is used in recovery of valuable colloidal materials from waste products, as spent catalysts[2]. Specific processes to remove pollution rely on air and water filtration with porous materials. In environmental engineering and geosciences, there is a remarkable interest in predicting how bio-colloids, such as viruses and bacteria, travel through soils or other porous matrices[3–5]. In addition, there is large evidence that disease outbreaks can take place when pathogens are not correctly filtered[6–9].

Natural, non-harmful colloids are also capable of enhancing the transport of dissolved soil pollution through porous media by passive stochastic motion[10,11]. In all these cases, a detailed knowledge of the porous matrix's morphology, and of the particle-matrix interactions is a key feature to completely understand the diffusion properties of colloidal species and how the confinement conditions influence the particles' motion. Recent works addressed these issues by studying the diffusion properties of colloids in quasi-2D confining networks[12–14]. As a result of 2D confinement, the particles' trajectories reveal the existence of two different states of motion: a free-diffusion state, typically associated to diffusion of particles in the bulk, unconfined part of the fluid, and a trapped state in which particles inside confining *holes* present sub-diffusive motion. Studies of transport within ordered 3D structures were able to show the effect of obstacles and structural constraints on colloids' motion[15–17]. In particular, a linear decrease of

* Corresponding author.
    *E-mail address:* emiliano.fratini@unifi.it (E. Fratini).
[1] G.B. and M.L. contributed equally to this work.
[2] ORCID: 0000-0001-8520-9919
[3] ORCID: 0000-0003-1334-5940
[4] ORCID: 0000-0001-7104-6530

diffusivity with increasing confinement length and with decreasing void volume fraction was reported[15–17]. However, the prediction of particle transport in disordered porous natural media requires additional, significant efforts. Important steps forward in this direction have been made by simulation studies[18,19]. The simplification of confining systems by considering regular, homogeneous, and geometrically isotropic pores, led to well-established relations that link the diffusion coefficient to the medium's porosity[20]. However, the extension of these approaches to anisotropic pore geometries could provide qualitative but no quantitative relation between diffusivity and porosity [20]. Experimental investigations remain scarce: only recently the effects of 3D confinement imposed by silica disordered porous media on nanoparticle transport were investigated[21], indicating a link between the decrease of void volume fraction and the slowing down of particle motions.

Overall, except for the model systems and the geometrically well-defined porous structures mentioned above, the simultaneous determination of the colloid dynamics and of the detailed 3D structure of the local porous environment is often difficult to be achieved experimentally. This is related to the fact that, while most of the application-relevant porous structures are opaque[22], the study of the colloid dynamics is usually performed through the application of optical methods, such as microscopy combined with particle tracking, or correlation techniques like dynamic light scattering and fluorescence correlation spectroscopy. The opacity of the matrix, due to the refractive index difference between the solid porous matrix and the fluid in its pores, often limits the tracking of colloidal probes in the proximity of the matrix surface, and thus no information on the 3D environment is available. One of the main strategies adopted to face these problems involves the so-called *index matching*[21,23,24], where the optical discontinuities can be cancelled by filling the pores with a liquid having a refractive index close to that of the solid porous matrix. In this case when light passes from the fluid to the solid matrix there is no reflection or refraction. This approach allows single particle tracking in porous media, however, losing the simultaneous acquisition of the structural information coming from the 3D matrix environment.

In the present work, we report on a simultaneous study of the local 3D porous structure of an application-relevant hydrogel matrix and the transport properties of soft colloidal particles absorbed in its interior. To this aim, we developed new poly (ethylene glycol)-based hydrogels with a highly interconnected micrometric porous structure and high transparency degree. Poly (ethylene glycol) (PEG) is the most commercially important polyether in terms of production volumes and it is used in several biomedical applications[25–28]. The cross-linking of polymeric units of PEG leads to hydrogels with a broad spectrum of physical and chemical properties. Starting from previous studies[29], we synthetized biocompatible hydrogels with optimal transparency. By freeze-drying treatment, we induced porosity at the microscale maintaining the desired transparency. The pores' size was tuned by changing the total amount of the structural component in the pre-reaction mixture. After rehydration of the xerogels, i.e. of the freeze-dried and completely dehydrated gel structures, the samples were analysed by laser scanning confocal microscopy (LSCM), scanning electron microscopy (SEM), and small-angle X-ray scattering (SAXS) to detail their structure from micro-to the nanoscale level. Laser scanning confocal microscopy allowed the 3D morphological and geometrical characterization of the different hydrogels. The study of the dynamics of soft thermo-sensitive poly-N-isopropylacrylamide (pNIPAM) colloids absorbed within the PEG hydrogel, obtained by particle tracking, was then quantitatively linked to the pore volume fraction and the geometrical features of the confining matrices.

## 2. Experimental section

### 2.1. Chemicals

Poly (ethylene glycol) (PEG) with molar weight of 35000 g/mol (purity 99%), acryloyl chloride (purity 97%), and 2,2-Dimethoxy-2-phenylacetophenone (DMP) (purity 97%) were purchased from Merck. As reported in the literature[29,30], the hydroxyl termini of PEG polymeric units were acrylated by 4-fold molar excess of acryloyl chloride and triethylamine in 100 mL of dichloromethane under a nitrogen atmosphere. The obtained poly (ethylene glycol) diacrylate (PEGDA) was precipitated out of the solution in cold diethyl ether. The filtered white powder was stored at − 20 °C until use. Oregon Green 488 (purity ≥95%) was purchased from ThermoFisher Scientific and used as received. N-isopropylacrylamide (NIPAM, purity 99%), N,N'-Methylenebis(acrylamide) (MBA, purity 99%), Ammonium persulfate (APS, purity ≥98%), and Rhodamine B (RhB, purity ≥95%) were purchased from Sigma Aldrich and used as received. Water was purified by a Millipore Milli-Q gradient system (resistivity >18 MΩ·cm).

### 2.2. PEG hydrogels preparation

Hydrogels' synthesis was carried out by radical photopolymerization of the acrylate polymeric units in water solution. The water-soluble polymer PEGDA can be easily cross-linked with a photosensitive initiator (such as DMP) to form a three-dimensional polymeric network[33,34]. The acrylic functionalities on both ends guarantee the three-dimensional crosslinking of the macro-monomer[35] (see SI, Fig. S1a). The two most common mechanisms used to explain the reticulation of a three-dimensional network from the linear polymer PEGDA are chain-growth and step-growth polymerization (see SI, Fig. S1b S1c). Chain-growth hydrogels result from the fast propagation of the active centres through monomers with unsaturated vinyl bonds (i. e. PEGDA or PEG dimethacrylate (PEGDMA)). This process results in a cross-linked high molecular weight chain. On the other hand, step-growth-polymerized hydrogels are formed by reaction of at least two multifunctional monomers with mutually reactive groups, where each monomer serves as a cross-linking point. In contrast to the chain-growth mechanism, step-growth gelation occurs when at least two multifunctional monomers react together producing fewer structural defects during reticulation. Generally, covalently crosslinked PEG hydrogels result from the combination of these two reaction mechanisms, leading to a more ordered structure, in the prevalence of step-growth, or with greater inhomogeneity, in the prevalence of chain-growth. The two mechanisms lead to a reticulated network with cross-linking points resulting from the combination of N active chains giving a N-folded chemical junction. In order to obtain pre-reaction mixtures with specific macro-monomer concentration (10, 12, 16, 20, 25, and 30 wt%), the appropriate amount of PEGDA was dissolved in water and mixed. Then, 10 µL of the DMP solution (0.2 g/mL) were added to the mixture and flushed with nitrogen for 1 min to remove dissolved oxygen that could interfere with the radical polymerization of PEGDA. The mixtures were centrifuged (3000 rpm for 10 min) to remove the entrapped bubbles and placed in rectangular demountable glass moulds of 2 mm of width. Then the mixtures were photo cross-linked overnight using a UV lamp (Camag®; power = 55 W; 365 nm wavelength) at a distance of 7.5 cm. After the polymerization, the hydrogels were cut into squares of 1 cm and kept in water until equilibrium was reached, replacing the water every 24 h. The swollen hydrogels were then lyophilized to induce the desired porosity by immersion in liquid nitrogen for 5 min and then dried at − 55 °C and 40 mtorr overnight. The ice crystals generated during the freezing process act as a porogen within the polymeric network. After the freeze-drying procedure, the gels were rehydrated in MilliQ water for 48 h. Hereinafter, all the hydrogels are named using the initial letter *"P"* followed by the macro-monomer concentration in the pre-reaction mixture. Under this notation the

investigated hydrogels fall in the range from P10 to P30.

## 2.3. pNIPAM micro-gels synthesis

Modified poly(N-isopropylacrylamide) microspheres of about 2 μm of mean diameter were prepared as previously described[2]. The microgels were labelled with Oregon Green 488 (OG) fluorescent dye that was added to the water solution of NIPAM. The mean diameter, the size distribution and thermal shrinking of the OG-pNIPAM microgels were investigated by dynamic light scattering (DLS) using a 90Plus particle size analyser (Brookhaven Instruments Corporation, BIC) with a wavelength of 659 nm and exploring a temperature range from 20° to 50°C. The size distribution and polydispersity were also confirmed by image analysis applied to optical microscopy images acquired at room temperature. The variation of the diameter as a function of temperature (see SI, Fig. S2a) was fitted through a sigmoidal curve indicating a maximum diameter of $1.8 \pm 0.1$ μm at T = 20 °C, which decreases to $0.99 \pm 0.05$ μm at T = 47 °C. For the same temperatures, the polydispersity index obtained from the DLS analysis was 0.20 and 0.06, respectively. The volumetric phase transition temperature resulted $32.3 \pm 0.1$ °C. Consistent with the DLS analysis, the image analysis of the optical micrographs at room temperature indicated a mean diameter of $1.8 \pm 0.2$ μm with a polydispersity index of 0.22 (see SI, Fig. S2b-c).

## 2.4. Characterization techniques

### 2.4.1. Swelling behaviour

The Equilibrium Water Content (EWC) is an essential parameter for the physico-chemical characterization of hydrogels, giving information on the hydrophilicity of the polymeric network[31]. We followed the water swelling kinetics of all the synthesized hydrogels by measuring their weight as a function of time, and we calculated the EWC and the hydration degree as follows[32,36]:

$$EWC = \frac{W_w - W_d}{W_w} \times 100 \qquad (1)$$

$$Hydration \quad Degree \quad = \frac{W_w - W_d}{W_d} \times 100 \qquad (2)$$

where $W_w$ and $W_d$ are the weights of the swollen and xerogel, respectively.

### 2.4.2. Differential scanning calorimetry

Differential scanning calorimetry (DSC) was carried out with a DSC 2500 Discovery (TA) instrument to determine the different states of water in the hydrogels[37,38]. The measurements were carried out at a constant nitrogen flow rate (i.e., 50 mL/min) of about 10–20 mg of sample loaded in a closed aluminium pan. The thermograms were acquired from $-60$ to 20 °C with a heating rate of 0.5 °C/min. The DSC system is automatically normalizing the heat flow by the initial weight of the sample. This practice does not yield misleading results since in our operational conditions the weight of the sample does not change during the experiment. In an equilibrated hydrogel, water molecules can be classified in three types: 'primary bound water', 'secondary bound water', and 'free water'[38–40]. The 'primary bound water' is formed by water molecules that directly bind to the hydrophilic groups of the polymer network and represents the non-freezable water fraction. The 'secondary bound water' fraction gathers the molecules of water "feeling" the polar groups because of the interaction with the primary bound water. After saturation of the hydrophilic and polar groups, all the extra water loaded in the hydrogel can be considered as 'free water' since it behaves as if it was in the bulk. Primary and secondary bound water are sometimes combined in a 'total bound water' fraction, simply called bound water. Applying a slow heating rate, it is possible to quantify these fractions. Experimentally, the 'free water' undergoes melting at the same temperature of bulk water (0 °C), while the melting

of the 'secondary bound water' takes place 10–40 °C below[38]. On the other hand, the 'primary bound water' does not undergo freezing even at $-70$ °C. According to the following equations, it is possible to determine the free and bound water index (FWI, BWI), and the free and secondary bound water mass for unit mass of polymer ($C_{fw}$ and $C_{bw}$ respectively):

$$FWI = \frac{\Delta H_{exp(T \approx 0 \ °C)}}{EWC \times \Delta H_{theo}} \qquad (3)$$

$$BWI = \frac{\Delta H_{exp(T < 0 \ °C)}}{EWC \times \Delta H_{theo}} \qquad (4)$$

$$C_{fw} = \frac{x_w \times FWI}{x_p} \qquad (5)$$

$$C_{bw} = \frac{x_w \times BWI}{x_p} \qquad (6)$$

### 2.4.3. Small-angle X ray scattering

SAXS analysis was carried out using a Xeuss 3.0 HR apparatus (Xenocs, France), equipped with an EIGER2R (1 M model) hybrid pixel photon counting detector (Dectris Ltd., Switzerland) consisting of $1028 \times 1062$ pixels with a size of $75 \times 75$ μm$^2$, which is free to move on a rail in a chamber under vacuum. The X-ray beam corresponds to the Kα radiation ($\lambda = 1.5406$ Å) emitted by a Cu microfocus sealed tube operated by a Genix 3D generator working at full power (i.e., 30 W). Calibration of the sample to detector distance was performed using silver behenate (d = 58.376 Å)[41]. The experiments were performed under vacuum to minimize the scattering from air, using two sample-to-detector distances, 500 and 1800 mm. The scattering profiles were obtained by merging the data collected at these two configurations, corresponding to a scattering vector, q, range from 0.004 to 0.55 Å$^{-1}$ (i.e., q=$4\pi/\lambda$ sin$\theta$, where $2\theta$ is the scattering angle). Hydrogels were analysed in sealed demountable cells using Kapton® foils as windows. Scattering curves were converted in absolute intensity (mm$^{-1}$), by measuring the scattering from a calibrated secondary standard (i.e., glassy carbon) in the same experimental conditions[42]. Finally, the 1-D azimuthal averaged scattering patterns were reduced, subtracting the scattering intensity from empty holder + water and merging the curves obtained at the two sample-to-detector distances. Data reduction, normalisation and merging was performed by using XSACT (X-ray Scattering Analysis and Calculation Tool) software (Xenocs, France).

### 2.4.4. Confocal and electron scanning microscopy

The micron-scale hydrogel structure was characterized by confocal laser scanning microscopy (CLSM) and scanning electron microscopy (SEM). All the samples were labelled with RhB by immersion in dye solution for at least 3 days. Thanks to the affinity between the fluorescent probe and the polymer, the RhB spontaneously labels the PEG structure by physical adsorption. CLSM imaging was carried out using a Leica TCS SP8 confocal microscope. Lab-Tek Chambers with N.1 borosilicate glass coverslips at the bottom were used as a sample holder. A $63 \times$ oil immersion objective with N.A. = 1.43 was used for the imaging of all samples. RhB was excited with a laser having a wavelength of 591 nm, and the fluorescence emission was acquired using a highly efficient hybrid detector in the $571 - 600$ nm range. 3D image stacks of $1024 \times 1024 \times 40$ pixels$^3$ were acquired, which correspond to hydrogel volumes of $90 \times 90 \times 40$ μm$^3$. The imaging was always performed on completely hydrated samples, before and after the freeze-drying procedure. SEM investigation on the freeze-dried and completely dehydrated samples (xerogels) was performed by means of a FEG-SEM ΣIGMA (Carl Zeiss, Germany) using an acceleration potential of 2 kV and a working distance of about 3 mm. Under these conditions, the metallization of the samples was not necessary.

*2.4.5. Morphological analysis of the porosity*

The volumetric image stacks acquired with confocal microscopy were processed and analysed using MorphoLibJ, a collection of mathematical morphology methods for ImageJ[43,44], to extrapolate structural, morphological and geometrical features of the porosity. The 3D scans acquired by CLSM were converted in binary 8-bit images and then optimized to apply the "distance transform watershed"[44]. This method can distinguish individual pores within the void space of the image stack, by disentangling touching pores. Once the pores were determined from the previously described analysis, their volume was calculated and used to obtain the pore volume fraction (Φ) of the hydrogel according to Eq. 7. This quantity is often reported as *porosity* in the literature. Pores on the edges were removed to avoid bias on the geometrical data processing.

$$\Phi = \frac{V_{pores}}{V_{tot}} \tag{7}$$

In the same plugin, the tool "analyze regions 3D" allowed the calculation of the characteristic geometrical parameters of the pores. The normalized sphericity index, defined as the ratio of the squared volume over the cube of the surface area, was calculated for each sample (see Eq. 8).

$$Sphericity = 36\pi \frac{V^2}{S^3} \tag{8}$$

Moreover, the tool returns the size and the orientation of each inertia ellipsoid that best fits within a pore, defined by the three characteristic lengths $R_1$, $R_2$, and $R_3$ (the three axes of the ellipsoid) in order of decreasing magnitude, as well as its elongation, defined as the ratios of the lengths: $R_1/R_2$, $R_1/R_3$, $R_2/R_3$. The obtained characteristic parameters were compared to the average pore diameter obtained, on the same images, through ImageJ software with the "count particles" method. This method was applied to 2D sections, at different heights, of the collected volumes and returned the area and the radius of the equivalent circle for each detected object.

*2.4.6. Particle tracking*

The same instrumental setup described for the 3D imaging was used for the particle tracking measurements. The RhB-labelled hydrogels were loaded with the fluorescent probe by immersion in the OG-pNIPAM microgel dispersions (2 wt%). The loading was carried out under mixing (300 rpm) at 35 °C for three days. During this process some leaking of the physically adsorbed dyes is possible. However, we did not find any significant effect of leaking on the imaging. Thanks to the pNIPAM thermal shrinking, the microgels could enter the interconnected porosity of the hydrogel. For each particle tracking experiment, time series of images of 512 × 512 pixels, corresponding to an area of approximately 50 × 50 μm$^2$ were investigated (the pixel size being 0.0903 μm). Images were acquired for 80 s with a frame interval of 0.03620 s. All measurements were conducted at room temperature. For comparison, a simple microgel dispersion was also measured under the same experimental conditions and used as reference. Movies of the diffusing particles in the x-y plane were analysed using Trackpy[45], a Python implementation of the widely-used Crocker-Grier algorithm[43], to obtain particle locations and trajectories. The software allowed the correction of any background drift, which might be due to large-scale flow or to any microscope stage movement. The ensemble mean squared displacement (MSD) of all particles was computed using the "emsd" function in Trackpy.

## 3. Results and discussions

### 3.1. Synthesis of the porous hydrogel and swelling characterization

The PEG hydrogels increase more than 300 times their mass during the swelling process in water, reaching the equilibrium water content in 24 h. After the lyophilization and rehydration process, all the samples showed slight opacity, as illustrated in Fig. S3a-b of the Supplementary Information, in which the hydrogels before (a) and after the process (b) were photographed while laying on top of a sketch of blue droplets. The small loss of transparency observed in Fig. S3b is due to the structural changes at the microscale, which induce a slight change in the refractive index. All the gels retained their elasticity after the structural changes.

The swelling characterization obtained from swelling curves (see SI, section 1.4) indicates a similar EWC for all samples, slightly decreasing with increasing the PEG macro monomer concentration. Results on the free and bound water states obtained from DSC are also reported and discussed in the SI, section 1.4.

### 3.2. Nanoscale topology and structure

SAXS experiments were carried out to investigate changes in the nanostructure of the gels associated with changes in the PEG content of the pre-reaction mixture. SAXS intensity distributions obtained for all samples are reported in Fig. 1a. The scattering profiles show a pronounced forward scattering indicating the presence of large-scale structures, and an inflection for q values approaching 0.1 $\mathring{A}^{-1}$. A generalized version of the Debye-Bueche model[31] was applied to fit the SAXS curves (Fig. 1a). This model is composed of two q-dependent contributions and an instrumental background[32]:

$$I(q) = I_{sol}(q) + I_{ex}(q) + bkg \tag{9}$$

The first term is the generic version of the Ornstein-Zernicke equation:

$$I_{sol}(q) = \frac{I_{lor}(0)}{[1 + (\zeta q)^m]} \tag{10}$$

where $I_{lor(0)}$ is the scattering intensity at q = 0, that depends only on the contrast between the polymer and the solvent and the volume fraction of the polymer in the gel, $\zeta$ is the characteristic average mesh size (or correlation length) of the network, and $m$ is the Porod exponent associated with the polymer-solvent interactions. The forward scattering at low q, associated to the solid-like inhomogeneities in the hydrogel, is described as:

$$I_{ex}(q) = \frac{I_{ex}(0)}{(1 + a^2 q^2)^2} \tag{11}$$

where $I_{ex}(0)$ is the excess intensity at $q = 0$ and $a$ is the length scale of the inhomogeneities in the polymeric structure of the gel. The fitting parameters derived from the modelling of the SAXS curves are listed in Table 1. As summarized in Fig. 1b, the average mesh size of the lyophilized-rehydrated samples follows an exponential decrease as a function of PEG content in the pre-reaction solution, going from about 8 nm at 10 wt% of PEG to about 2 nm at 30 wt% of PEG. This also means that $\zeta$ decreases with decreasing pore volume fraction.

Consistent with expectations, the Porod exponent *m* increases with increasing PEG content, suggesting a collapsing polymeric network. The Porod exponent reflects the local morphology of the network and is a strong marker of the interactions taking place between the polymeric chains and the solvent. In particular, it is well-known that *m* = 1.67 for linear polymer coils in good solvent conditions and reaches 2 in the case of a *theta* solvent[46], where the polymer-polymer interactions are comparable to the polymer-solvent interactions. To simplify this point, *m* decreases as the polymer network expands and increases when the polymer network collapses. The macro-monomer concentration determines the mechanical properties of the gel after the polymerization and its resistance to the structural deformation performed by the ice crystals during the freeze-drying treatment applied to sculpt the final porosity in the hydrogel. The growing ice crystals act as pore formers, collapsing the polymeric chains while enhancing the polymer-polymer
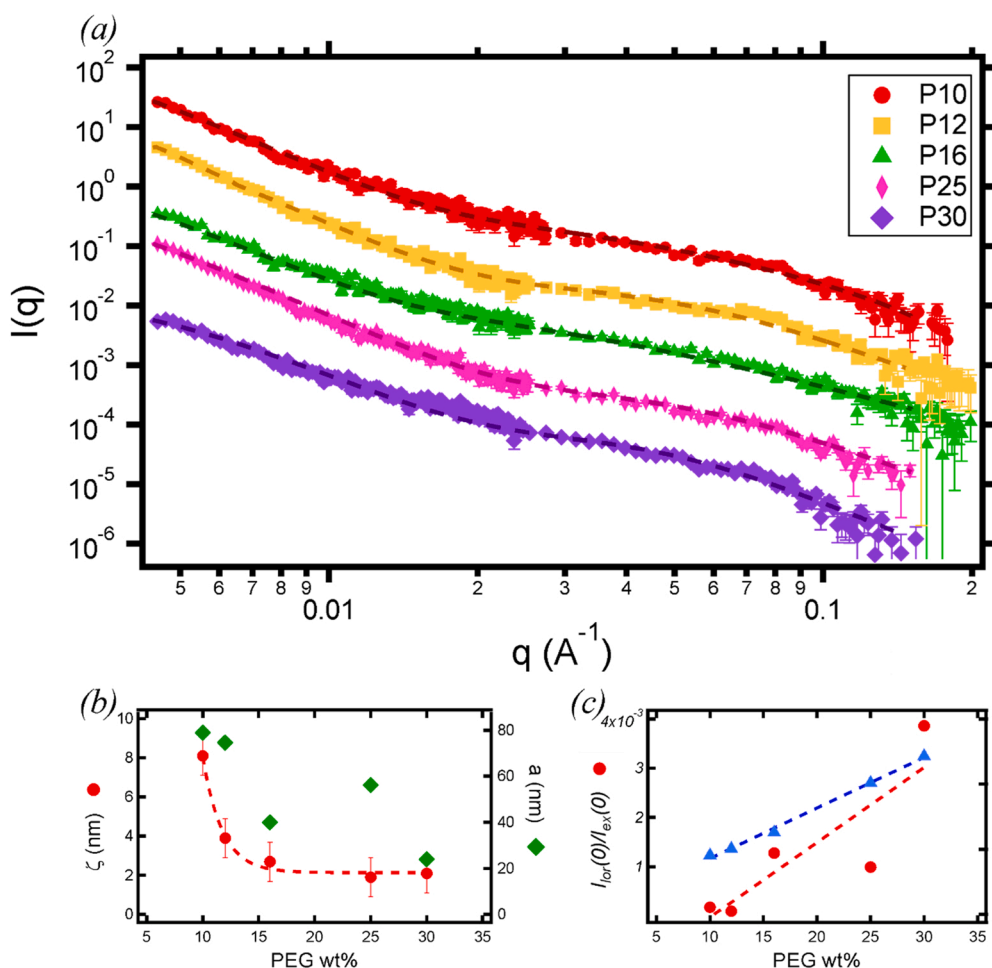
**Fig. 1.** SAXS profiles of the porous hydrogels in their hydrated state (a). Fitting curves are reported as dotted lines together with the experimental data (full markers). The curves are offset along y-axes for clarity. Average mesh size and solid-like in-homogeneities of the PEG hydrogels as a function of the structural component in the pre-reaction mixture (b). The scattering intensities ratio and the Porod exponent as a function of the structural component (c). The scattering in-tensities ratio gives the relative popu-lation distribution of the "open" polymeric network and solid-like in-homogeneities, while the Porod expo-nent reflects the polymer-polymer/ polymer-solvent interactions.

**Table 1**

Fitting parameters obtained from the modeling of the SAXS curves modelling for the different PEG hydrogels according to Eqs. (9–11).

| Sample | $I_{lor}(0)$ ($10^{-2}$) | $\zeta$ (nm) | $m$ | $I_{ex}(0)$ | $a$ (nm) |
|--------|--------------------------|--------------|-----|-------------|----------|
| P10 | $4.08 \pm 0.01$ | $8.1 \pm 0.5$ | $1.91 \pm 0.05$ | $233.4 \pm 0.2$ | $78.9 \pm 0.8$ |
| P12 | $1.42 \pm 0.01$ | $3.9 \pm 0.5$ | $2.01 \pm 0.02$ | $353.3 \pm 0.2$ | $74.6 \pm 0.8$ |
| P16 | $1.08 \pm 0.02$ | $2.7 \pm 0.5$ | $2.26 \pm 0.02$ | $8.49 \pm 0.1$ | $29.9 \pm 0.7$ |
| P25 | $0.5 \pm 0.1$ | $1.9 \pm 0.5$ | $3.02 \pm 0.02$ | $12.9 \pm 0.5$ | $59.2 \pm 0.7$ |
| P30 | $0.8 \pm 0.1$ | $2.1 \pm 0.5$ | $3.43 \pm 0.01$ | $2.1 \pm 0.4$ | $24.9 \pm 0.7$ |

interactions and reducing the polymer-solvent interactions similar to what was observed for PVA cryogels[47]. As a result of this phenome-non, the samples with higher macro-monomer content present larger Porod exponents. The initial value of 1.91 for P10 and similar values for P12 and P16 suggest a polymeric network where chains are in a con-dition similar to theta solvent (m=2). Increasing the PEG content, the Porod exponent increases reaching the value of 3 for 25 wt% of PEG in the pre-reaction solution. This situation reflects a completely collapsed system where the interaction with the solvent is minimized. The higher value found for P30 indicates a transition from a mass fractal to a surface fractal system.

On the other hand, the PEG content affects the size of the solid-like inhomogeneities in the gel, as indicated by the decrease of their average size (see $a$ value) with increasing PEG content, in agreement with the collapse phenomenon described by the $m$ exponent. The ratio ($I_{lor}(0)/I_{ex}(0)$, see Fig. 1c) can be finally used to estimate the relative weight of the scattering from the meshes of the polymer network with respect to the solid-like inhomogeneities, and reveals an increasing

trend with the macro-monomer content in the pre-reaction mixture; this is consistent with the increasing compactness of the hydrogel.

### 3.3. Morphological and geometrical characterization at the microscale

The heterogeneities of each sample were probed by LSCM and SEM. LSCM images of hydrogels acquired before freeze-drying confirmed the importance of the cryo treatment to induce porosity at the microscale, since no porosity could be detected in these samples (see Fig. S6). Confocal images in Fig. 2 illustrate the effect of the PEG concentration on the pore morphology and pore size after lyophilization and rehy-dration. As it can be seen, there is a progressive reduction of the pore size with increasing PEG content up to 20 wt%, while for larger values the gel network becomes suddenly more compact, and the pores are smaller and appear as localized inhomogeneities in the structure. SEM mea-surements of the xerogels (see SI Fig. S5) confirmed these findings. The quantitative analysis of 2D images allowed us to obtain a first estimate of pore sizes, through the average 2D pore diameter $\langle d \rangle$. This analysis (see Fig. 3a) shows that $\langle d \rangle$, consistently with the qualitative observations, decreases from 12 to 6.5 μm when the PEG macro-monomer concen-tration in the pre-reaction mixture increases from 10 to 20 wt%. The reduction is approximately linear. Beyond 20 wt% PEG content, the resulting network is poorly interconnected, and the visible pores reach a constant diameter $\langle d \rangle \approx 5$ μm. Moreover, crucial information on the 3D structure and morphology of the pores in the hydrogels was obtained from the image stacks. MorphoLibJ[44] was used to distinguish and characterize each pore in the hydrogel's structure within the image stack. As shown in Fig. 3b, after the processing performed in Morpho-LibJ, each pore was labelled with a different colour and analysed to
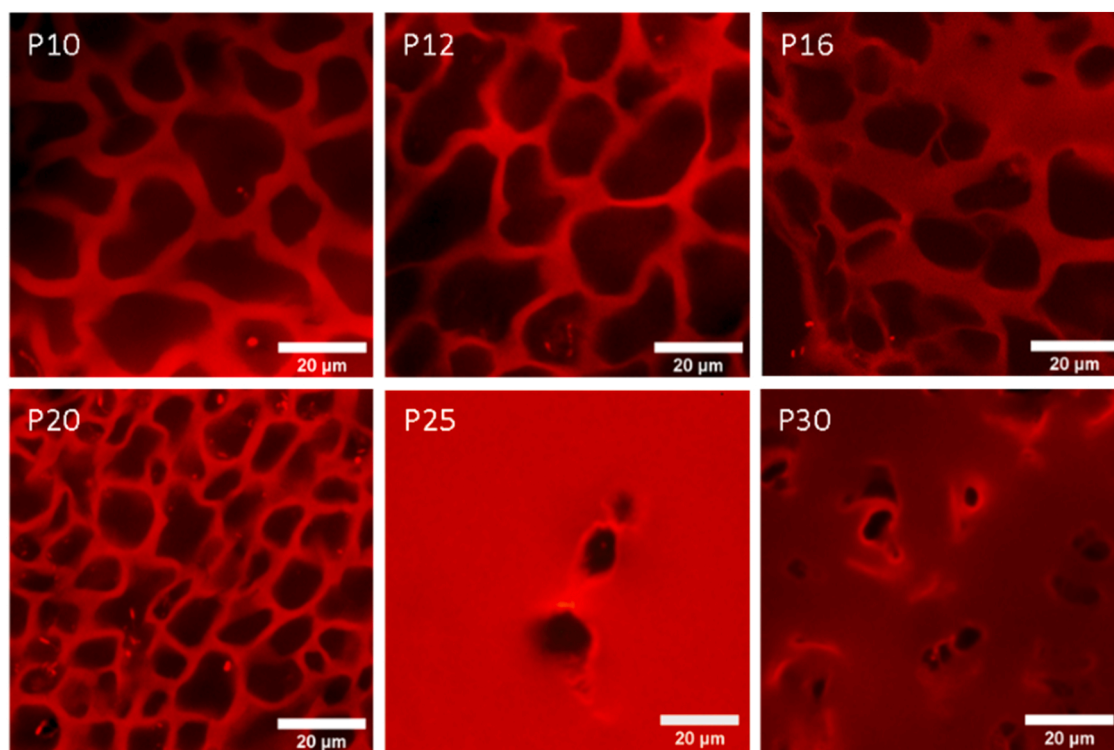
**Fig. 2.** LSCM micrographies of the rehydrated gels after freeze-drying treatment, for different macro-monomer contents.

determine the pore volume fraction (Eq. 7) and the geometrical features of the pores (Eqs. 8 and 9). Samples with a PEG content of 10 wt% presented an average pore volume fraction of 63%, which was reducing linearly to 48% for PEG content of 20 wt%. Consistent with the saturation of the pore size already evidenced in the 2D analysis, the linear relation between pore volume fraction and PEG content disappeared above 20 wt% of PEG content. Beyond this threshold the pore volume fraction in the polymeric network is dramatically reduced to 7% and 4% for PEG content of 25 and 30 wt%, respectively. As already mentioned, the structure of these two hydrogels appeared more compact (Fig. 2), presenting few pores without clear interconnection. The 3D analysis of the pore volume fraction confirms thus the presence of a small fraction of pores, supporting the interpretation that the high content of PEG does not allow the generation of a completely interconnected porous network.

Characteristic geometrical features, such as the sphericity index (Eq. 8) and the pores' elongation (Eq. 9), were extrapolated from the 3D images. Note that for estimating the elongation parameters, the size of the pores in the three cartesian directions, 1, 2 and 3, were computed for each pore. To obtain reliable data, pores on the edges of the image were excluded from the geometrical analyses. As summarized in Fig. 4, the geometrical parameters reported in Table 2 reveal the presence of channel-like pores elongated in the 1 direction (see Fig. 3c for an illustration of the reference system). The pores also present a relatively pronounced asymmetry in the 2–3 plane, with elongation along 2. Even if the elongation ratios are not significantly changing with increasing PEG content, except possibly for the 20 wt% sample, this does not mean that the pore structure is not affected. Increasing the PEG content in the pre-reaction mixture, smaller and narrower pores' elongation distributions are observed (see Fig. 5). Moreover, when less pores are present, they show a more self-similar shape. These geometrical features are related to the porogen agent used to induce the desired porosity (i.e., ice crystal)[48,49] which effect is drastically reduced as the concentration of PEG in the pre-mixture becomes larger than 25 wt%.

### 3.4. Particle tracking

The OG-pNIPAM microgels were synthesized as reported in previous studies[37,50], their characteristic dimension and thermal shrinking were determined by DLS and confirmed by optical microscopy (see SI file, Fig. S2). The mean diameter of the microgel particles at room temperature is equal to $1.79 \pm 0.02$ μm. A water dispersion of microgels at 2 wt% concentration was used for diffusion studies. As explained in the experimental section, the operating conditions of temperature and agitation allowed the loading of the microgels in the porous networks (see SI). Representative 2D images and 3D stacks of the diffusing pNIPAM particles loaded into the polymeric networks are reported in SI, Fig. S7a-b and c-d, respectively. Moreover, the dynamics were studied in the 2–3 plane (see Fig. 3a), since the acquisition speed of the confocal microscope was not sufficient to follow the particle dynamics in 3D, at least for the less confined systems. This is evidenced by the deformation of the particles in the 3D stacks of Fig. S7c-d, which can be attributed to the fact that the particles move during the volume scan. However, due to the elongated structure of the pores evidenced in the previous section, with the pores which are significantly more extended in the direction perpendicular to the 2–3 plane (axis 1), we expect that the effect of confinement should be revealed by the in-plane dynamics. Representative videos of the diffusing pNIPAM particles, in unconfined and confined conditions, are reported in the SI. The particle tracking method allowed the determination of the microgel dynamics in all the investigated systems. The diffusive motion parameters were successfully extrapolated from the log-log plot of the mean square displacement (MSD) as a function of the lag-time ($\tau$), shown in Fig. 6. These data were obtained by averaging the 2D trajectories of all the diffusing particles over all the initial times. The averaged MSD is thus defined as:

$$\langle \Delta r^2_{(\tau)} \rangle = \langle \left[ x_{(t+\tau)} - x_{(t)} \right]^2 + \left[ y_{(t+\tau)} - y_{(t)} \right]^2 \rangle_{i,t} \tag{12}$$

where x and y are the time-dependent coordinates of the centroid representing the diffusing particle and $\langle \rangle_{i,t}$ indicates an average over many starting times for the ensemble of all microspheres in the field of view. $\tau$
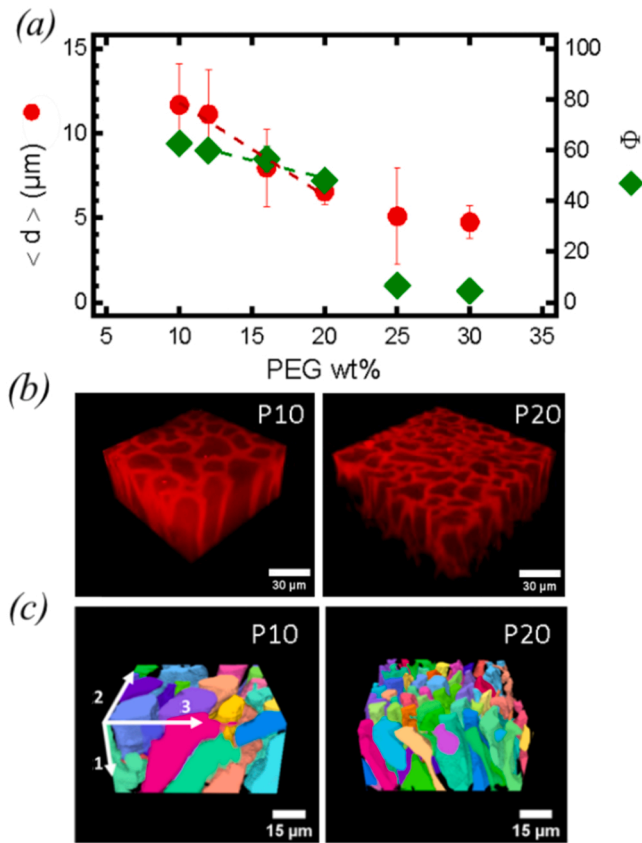
**Fig. 3.** The pore mean diameter ($<d>$) and pore volume fraction ($\Phi$) extrapolated from the 2D, and 3D images analysis were plotted as a function of the macro-monomer concentration in the pre-reaction mixture (a). 3D images of the porous hydrogels P10 and P20 obtained from the LSCM micrographies (b) and processed with MorphoLibJ (c). The reference axes 1, 2, 3 are reported on the left image of (c).

is the lag-time between two positions of a particle along a trajectory used to calculate the MSD. Sufficiently dilute micron-sized spheres dispersed in a Newtonian fluid of viscosity η should undergo simple Brownian motion[51–53] with a diffusion coefficient $D_0$ given by the Stokes-Einstein relation:

$$D_0 = \frac{kT}{6\pi\eta R} \tag{13}$$

where $R$ is the radius of the diffusing particle, $k$ is the Boltzmann's constant, and $T$ is the temperature in K. At sufficiently long times compared to the Brownian diffusion time, $\tau_B = R^2/D_0$, the lag-time dependence of the 2D MSDs can be written as:

$$\langle \Delta r^2_{(\tau)} \rangle = 4D_{eff}\tau^n \tag{14}$$

where $D_{eff}$ is an effective diffusion coefficient and the exponent $n$ is related to the nature of particle displacements. For $n = 1$ the motion is defined as diffusive, while for $n$ smaller than 1, it becomes sub-diffusive.

The dynamics of the pNIPAM particles were studied in unconfined conditions by the direct analysis of the microgels' water dispersion. The MSDs of the microgels in unconfined and confined conditions are reported in Fig. 6. The progressive decrease of the MSD because of the increasing confinement conditions imposed by the hydrogel matrices is clearly observable in the figure. The analysis of the MSD using Eq. 14 revealed a sub-diffusive motion for all samples in which the microgels are confined within the porous polymeric network. Consistent with the imposed confinement, the exponent $n$ and the effective diffusion coefficient depend on the hydrogel's porosity. The extrapolated
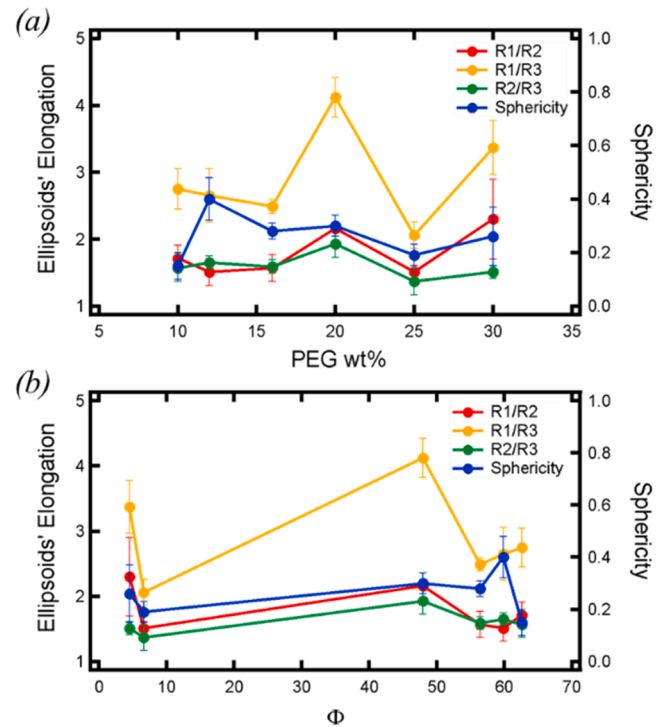


**Fig. 4.** Characteristic geometrical parameters of the pores in the hydrogels' network as a function of PEG content in the pre-reaction mixture (a), and the pore volume fraction $\Phi$ (b).

**Table 2**
Characteristic geometrical parameters of the pores in the PXX hydrogels' network (XX is the wt% of PEG in the pre-reaction mixture).

| Sample | $\Phi$ (%) | Sphericity | R1/R2 | R1/R3 | R2/R3 |
|---|---|---|---|---|---|
| P10 | 62.6 | 0.15 ± 0.05 | 1.7 ± 0.2 | 2.8 ± 0.3 | 1.6 ± 0.2 |
| P12 | 59.9 | 0.40 ± 0.08 | 1.5 ± 0.2 | 2.7 ± 0.4 | 1.6 ± 0.1 |
| P16 | 59.4 | 0.28 ± 0.03 | 1.6 ± 0.2 | 2.5 ± 0.1 | 1.6 ± 0.1 |
| P20 | 48.0 | 0.30 ± 0.04 | 2.2 ± 0.2 | 4.1 ± 0.3 | 1.9 ± 0.2 |
| P25 | 6.6 | 0.19 ± 0.04 | 1.5 ± 0.1 | 2.1 ± 0.2 | 1.4 ± 0.2 |
| P30 | 4.5 | 0.26 ± 0.10 | 2.3 ± 0.6 | 3.4 ± 0.8 | 1.5 ± 0.1 |

characteristic parameters are reported in Table 3. The maximum values of $n$ and D, 0.60 and 0.17 μm²/s, respectively, were found for the microgels loaded in the hydrogel with the largest pore diameter and pores' volume fraction (corresponding to hydrogel P10). These quantities gradually decrease for larger PEG fraction, attaining values of 0.24 and 0.11 μm²/s for P20. Samples with higher content of PEG present a smaller number of pores with relatively small sections and a small degree of interconnection, with the result that the dynamics of the particles in these gels is strongly reduced. The particles loaded in these last systems are indeed presenting small displacements and are almost stuck in the few holes within the polymer network. Therefore, for these samples, due to the strong sub-diffusive behaviour of the MSD, the obtained effective diffusion coefficients are not entirely reliable and most likely overestimate the particle mobility. Fig. 7 shows the effective diffusion coefficient, $D_{eff}$, and the exponent, $n$, normalized by the corresponding values obtained for the unconfined dispersion (i.e., $D_{eff}^0$ and $n^0$) as a function of the geometrical parameters describing the porous structure. These include the normalized confinement length ($\xi$) and the particle area fraction ($\alpha$) of the diffusing particles loaded in the different polymeric matrices, which are defined as follows:

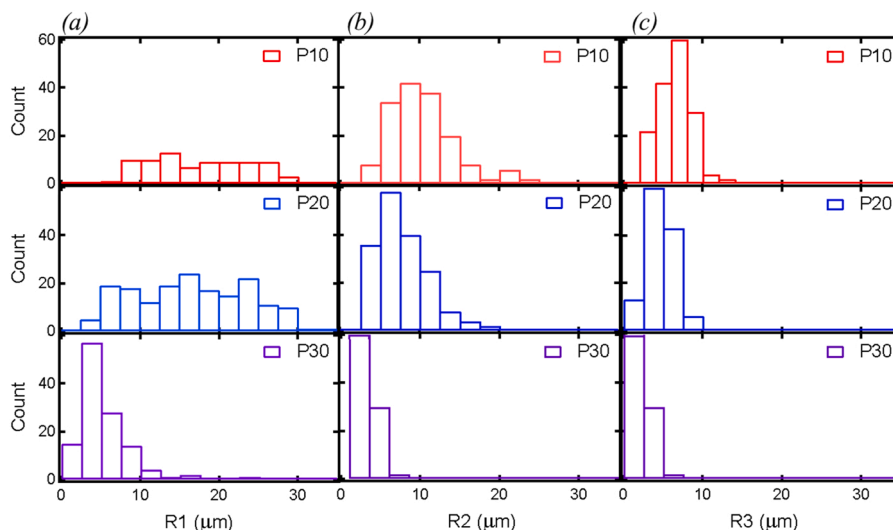$$\xi = \frac{d_{particle}}{d_{pore}} \tag{15}$$

**Fig. 5.** Distribution of the length of the axes of the ellipsoids used to model the pore volumes, R1(a), R2 (b), and R3(c) in the different gels P10, P20, P30.
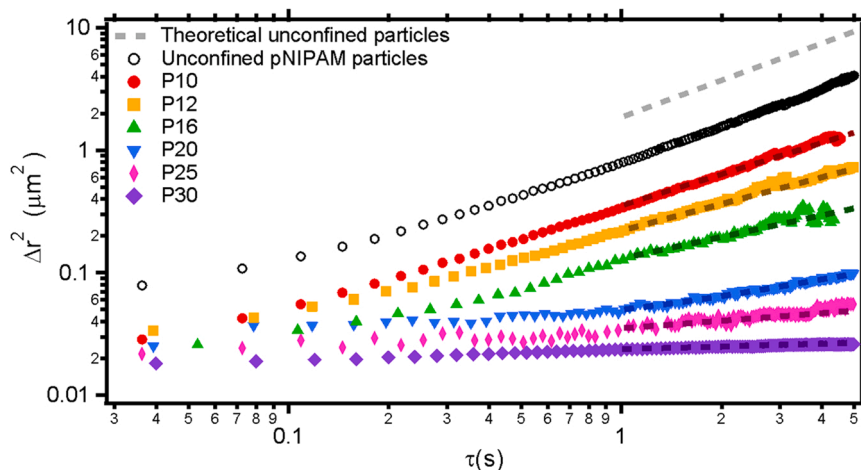


**Fig. 6.** Mean Square Displacement of the diffusing pNIPAM microgels in unconfined conditions and loaded in the different porous hydrogels. Fitting curves are reported as dotted lines together with the experimental data (full and empty markers for the confined and the unconfined conditions).

**Table 3**
Diffusion exponent n and the effective diffusivity for the pNIPAM particles in PXX hydrogels compared to confinement hydrogels' parameters Φ, ξ, and α (XX is the wt% of PEG in the pre-reaction mixture).

| Sample | Diffusion exponent $n$ | Diffusivity ($\mu m^2/s$) | Φ | ξ | α |
|---|---|---|---|---|---|
| P30 | $0.19 \pm 0.03$ | $0.04 \pm 0.02$ | 4 | 0.38 | 0.29 |
| P25 | $0.20 \pm 0.01$ | $0.09 \pm 0.003$ | 7 | 0.35 | 0.28 |
| P20 | $0.24 \pm 0.06$ | $0.11 \pm 0.03$ | 48 | 0.29 | 0.11 |
| P16 | $0.38 \pm 0.08$ | $0.13 \pm 0.03$ | 59 | 0.23 | 0.08 |
| P12 | $0.46 \pm 0.11$ | $0.15 \pm 0.03$ | 59 | 0.17 | 0.07 |
| P10 | $0.60 \pm 0.05$ | $0.17 \pm 0.01$ | 63 | 0.15 | 0.04 |
| Non-confined system | $0.96 \pm 0.002$ | $0.38 \pm 0.005$ | – | – | – |
| Theoretical Value (Non-confined system) | 1.00 | 0.42 | – | – | – |

$$\alpha = \frac{A_{particles}}{A_{pore}} = \frac{n_{particles} * A_{single\ particle}}{A_{pore}} \qquad (16)$$

where $d_{particle}$ and $d_{pore}$ are the particle and pore diameter while, $A_{particles}$ and $A_{pore}$ are the total particles and pores area in the investigated image. The total particles' area was determined from the number of particles in

the investigated area ($n_{particles}$) multiplied by the area of the single pNI-PAM particle ($A_{single\ particle} = \pi R^2$). In addition, we consider the pore volume fraction defined in Eq. 7.

Consistent with previous results on nanoparticles moving through model, structured and unstructured porous media[15,21,54–56], we found that the normalized effective diffusivity and power-law exponent decrease as $\xi$ and $\alpha$ increase over the entire investigated range (see Fig. 7a). The value of $D_{eff}/D_{eff}^0 \approx 0.44$ at $\xi \approx 0.15$ obtained for our system is slightly smaller than those obtained in previous studies on the diffusion of nanoparticles in unstructured porous media composed of packed beds of glass beads[52] or polymer films[22], in which $D_{eff}/D_{eff}^0 \approx 0.53$ and 0.50, respectively. This indicates slightly more pronounced confinement effects imposed by the hydrogel matrix. In ref. [52] the experimental results were interpreted in terms of matrix mediated steric and hydrodynamic effects, by comparing with analytical models that describe these effects for cylindrical[57–61] and slit-like pores[62,63]. Using the morphological analysis of the internal porosity, which indicates channel-like pores, we compared the dependence of $D_{eff}/D_{eff}^0$ on $\xi$ with the model which is expected to predict more accurately steric and hydrodynamic effects in cylindrical pores[59]. The results of the comparison, which has no adjustable parameters, are
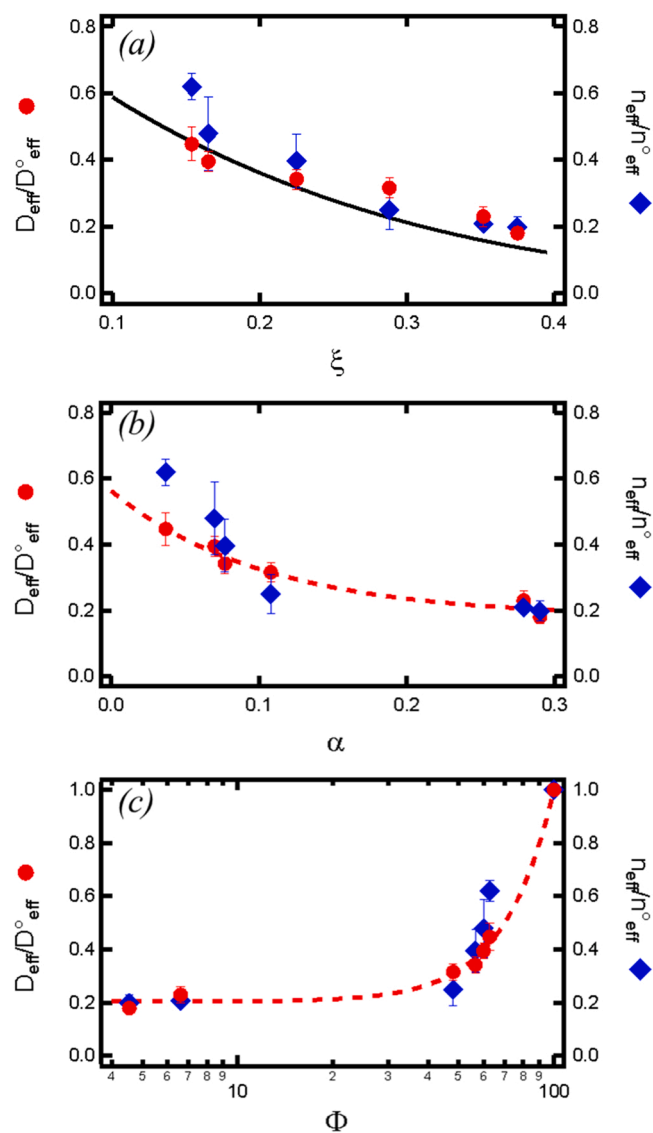
**Fig. 7.** Normalized effective Diffusivity and Power-law exponent of the pNI-PAM microgels as a function of the normalized confinement length (a) and the pore volume fraction (b). The normalized parameters were plotted as a function of the pore volume fraction (c) and the particle area fraction. The continuous line in (a) represents a model calculation for diffusion in cylindrical pores that includes steric and hydrodynamic effects [59]. Dashed lines in (b) and (c) are fits to a power-law and an exponential dependence, respectively, as detailed in the text.

reported in Fig. 7a and show a semi-quantitative agreement between model and data, with the model that slightly overestimates the effects of confinement for the larger $\xi$ values, where however the experimental values of $D_{eff}/D_{eff}^0$ might be also slightly overestimated, as already commented. The good qualitative agreement between experiments and predictions suggests that for our system the hydrodynamic and steric effects play a major role in the reduction of diffusivity. The effective diffusion coefficient and power-law exponent also present a decrease as a function of the particle area fraction $\alpha$, which is pronounced for small $\alpha$ values and becomes milder for $\alpha > 0.1$ (see Fig. 7b). Note that the critical area fraction $\alpha = 0.1$ at which the particles present a very limited mobility is relatively small, confirming that, in addition to geometric confinement, effects like hydrodynamic interactions or a non-uniform absorption of particles affect the dynamics. The reduction of $D_{eff}/D_{eff}^0$ as a function of $\alpha$ can be described with a power-law with exponent

$-0.38 \pm 0.05$.

Fig. 7c shows the dependence of $D_{eff}/D_{eff}^0$ and $n_{eff}/n_{eff}^0$ on the pore volume fraction, often called porosity. Consistent with Fig. 7b, the parameters are almost constant up to $\Phi = 0.4$, while they increase for larger $\Phi$ values. The relationship between $D_{eff}/D_{eff}^0$ and $\Phi$ could be described by a power-law dependence with an exponent $2.7 \pm 0.2$. Note that the experimental relationship between the effective diffusion coefficient and 3D porosity for particles confined in random porous media has never been reported due to the difficulty of characterizing the pore volume in such systems. We can compare the obtained exponent with results for gas diffusion in porous media, where however the effects of a comparable particle-pore size and steric and hydrodynamic effects are not considered. A variety of models for pores with different geometries describe dependencies of $D_{eff}/D_{eff}^0$ vs $\Phi$ with power-law exponents that never exceed 2[20]. The larger exponent found in our case, which indicates a stronger effect of confinement, supports the important influence of hydrodynamic and steric effects for finite size particles, and possibly indicates the role of interactions between the particles and the hydrogel matrix. A more detailed understanding of the origin of the observed relationship needs additional insight that will be the subject of future work. To obtain further information about the process controlling the confined dynamics of the particles in the different confining structures, we analysed the one-dimensional particle displacements distributions $\Delta G_s(\Delta r, \Delta t)$ at different lag times in the different confining structures. Consistent with the confinement imposed by the pores, the distribution of the particle displacements became narrower for gels with a higher PEG fraction. The distributions of the particle displacements are approximately Gaussian in the confining structures P10 and P12, while for samples P16 and P20 deviations from Gaussian behaviour are already present (see Fig. S8 in the SI).

## 4. Conclusions

The development of PEG hydrogels with a high degree of transparency and a fluorescently labelled polymer network allowed us to investigate the dynamics of microgels in disordered 3D porous confinement. The internal porous structure was obtained by freeze-thawing and could be modulated through the macro-monomer content in the pre-reaction mixture. Combining different experimental techniques, including SAXS, SEM and confocal microscopy, the internal porous structure of the hydrogels was characterized in detail. In particular, the analysis of 3D image stacks obtained by confocal microscopy using MorpholibJ provided volumetric information on the pore geometry as a function of PEG content. The results of the analysis revealed a highly asymmetric channel-like porosity, in which the increase of PEG content induces a progressive reduction of the channels' section. This decrease was found to be linear up to a critical threshold of 20 wt% PEG content, after which the porosity and the pore interconnection dramatically decrease.

Particle tracking analysis of the displacements of microgels absorbed within the hydrogel matrices highlighted the effects of confinement on the transport of the microgels. The dynamics of the microgels changed from approximately diffusive inside broad channels to sub-diffusive in narrow channels, in agreement with results obtained for nanoparticles confined in inverse opal structures. Exploiting the results of the 3D morphological analysis of the porosity, that indicates the presence of elongated, channel-like pores, we compared the dependence of the effective diffusion coefficient on the confinement length with models for diffusion of particles in cylindrical pores, that consider hydrodynamic and steric effects. The good agreement between our findings and model predictions indicates the importance of these effects on the confined microgel dynamics. Additionally, we found that the effective diffusion coefficient presents a strong dependence on the pore volume fraction, which could be described through a power law dependence with an exponent significantly larger than those expected for pure geometrical

confinement effects imposed by porous random media. This confirms the presence of additional effects, such as the already mentioned hydrodynamic and steric interactions, as well as the possible influence of microgel-hydrogel matrix interactions.

Our results highlight the importance of a detailed morphological characterization of the porosity in disordered confining matrices to understand the effects of confinement on the transport of particles, with important implications in micro and nanofiltration, anti-bacterial and anti-viral strategies, selective absorption, among others.

## CRediT authorship contribution statement

**Gavino Bassu:** Investigation; Data curation; Formal analysis; Methodology; Visualization; Writing – original draft; Writing – review & editing, **Marco Laurati:** Conceptualization; Data curation; Formal analysis; Methodology; Validation; Writing – original draft; Writing – review & editing, **Emiliano Fratini:** Conceptualization; Funding acquisition; Project administration; Methodology; Resources; Supervision; Validation; Writing – review & editing.

## Declaration of Competing Interest

The authors declare that they have no known competing financial interests or personal relationships that could have appeared to influence the work reported in this paper.

## Data Availability

Data will be made available on request.

## Acknowledgment

*Author contributions*

The manuscript was written through contributions of all authors, and all authors have given approval to the final version of the manuscript.

*Notes*

The authors declare no competing financial interests.

*Associated content*

*Supporting information*

Details for: PEGDA polymerization, dyed pNIPAM microgels synthesis, swelling kinetics and water states, Scanning Electron Microscopy of xerogels, Exemplary LSCM images and videos used for particle tracking, 1D particle displacement distributions obtained from particle tracking. Supplementary Figs. S1-S8. Supplementary movies showing the particle dynamics under different confinement conditions.

## Appendix A. Supporting information

Supplementary data associated with this article can be found in the online version at doi:10.1016/j.colsurfb.2022.112938.

## References

[1] M. Rhodes, Introduction to Particle Technology, Wiley, 2008, https://doi.org/10.1002/9780470727102.

[2] J.E. Hoffmann, Recovery of platinum-group metals from gabbroic rocks metals from auto catalysts, JOM 40 (1988) 40–44.

[3] D.N. Thornlow, E.L. Brackett, J.M. Gigas, N. Van Dessel, N.S. Forbes, Persistent enhancement of bacterial motility increases tumor penetration, Biotechnol. Bioeng. 112 (2015) 2397–2405, https://doi.org/10.1002/bit.25945.

[4] Rd. Souza, R. Ambrosini, L.M. Passaglia, Plant growth-promoting bacteria as inoculants in agricultural soils, Genet Mol. Biol. 38 (2015) 401–419, https://doi.org/10.1590/S1415-475738420150053.

[5] G.A. Turnbull, J.A.W. Morgan, J.M. Whipps, J.R. Saunders, The role of bacterial motility in the survival and spread of Pseudomonas fluorescens in soil and in the attachment and colonisation of wheat roots, FEMS Microbiol. Ecol. 36 (2001) 21–31, https://doi.org/10.1111/j.1574-6941.2001.tb00822.x.

[6] A. Gallay, H. De Valk, M. Cournot, B. Ladeuil, C. Hemery, C. Castor, F. Bon, F. Mégraud, P. Le Cann, J.C. Desenclos, Outbreak Investigation Team, A large multi-pathogen waterborne community outbreak linked to faecal contamination of a groundwater system, France, 2000, Clin. Microbiol Infect. 12 (2006), 591–70.

[7] T.-T. Fong, L.S. Mansfield, D.L. Wilson, D.J. Schwab, S.L. Molloy, J.B. Rose, Massive microbiological groundwater contamination associated with a waterborne outbreak in Lake Erie, South Bass Island, Ohio, Environ. Health Perspect. 115 (2007) 859–864, https://doi.org/10.1289/ehp.9430.

[8] E.K. Wallender, E.C. Ailes, J.S. Yoder, V.A. Roberts, J.M. Brunkard, Contributing factors to disease outbreaks associated with untreated groundwater, Ground Water 52 (2014) 886–897, https://doi.org/10.1111/gwat.12121.

[9] J. Abu-Ashour, D.M. Joy, H. Lee, H.R. Whiteley, S. Zelin, Transport of microorganisms through soil, Water Air. Soil Pollut. 75 (1994) 141–158, https://doi.org/10.1007/BF01100406.

[10] P.W. Reimus, M. Zavarin, Y. Wang, Colloid-Facilitated Radionuclide Transport: Current State of Knowledge from a Nuclear Waste Repository Risk Assessment Perspective, Los Alamos, NM (United States), 2017. https://doi.org/10.2172/1341822.

[11] M. Ryan, J.N. Elimelech, Colloid mobilization and transport in groundwater, Colloids Surf. A 107 (1996) 1–59.

[12] D. Nykypanchuk, H.H. Strey, D.A. Hoagland, Brownian motion of DNA confined within a two-dimensional array, Science 297 (2002) 987–990, https://doi.org/10.1126/science.1073277.

[13] W.D. Volkmuth, R.H. Austin, DNA electrophoresis in microlithographic arrays, Nature 358 (1992) 600–602, https://doi.org/10.1038/358600a0.

[14] D.M. Tartakovsky, M. Dentz, Diffusion in porous media: phenomena and mechanisms, Transp. Porous Media 130 (2019) 105–127, https://doi.org/10.1007/s11242-019-01262-6.

[15] K. He, F. Babaye Khorasani, S.T. Retterer, D.K. Thomas, J.C. Conrad, R. Krishnamoorti, Diffusive dynamics of nanoparticles in arrays of nanoposts, ACS Nano. 7 (2013) 5122–5130, https://doi.org/10.1021/nn4007303.

[16] R. Raccis, A. Nikoubashman, M. Retsch, U. Jonas, K. Koynov, H.J. Butt, C.N. Likos, G. Fytas, Confined diffusion in periodic porous nanostructures, ACS Nano. 5 (2011) 4607–4616, https://doi.org/10.1021/nn200767x.

[17] L. Ning, P. Liu, F. Ye, M. Yang, K. Chen, Diffusion of colloidal particles in model porous media, Phys. Rev. E. 103 (2021) 22608, https://doi.org/10.1103/PhysRevE.103.022608.

[18] J.A. Currie, Gaseous diffusion in porous media. Part 2. - Dry granular materials, Br. J. Appl. Phys. 11 (1960) 318–324, https://doi.org/10.1088/0508-3443/11/8/303.

[19] F.R. Troeh, J.D. Jabro, D. Kirkham, Gaseous diffusion equations for porous materials, Geoderma 27 (1982) 239–253, https://doi.org/10.1016/0016-7061(82)90033-7.

[20] N. Ray, A. Rupp, R. Schulz, P. Knabner, Old and new approaches predicting the diffusion in porous media, Transp. Porous Media 124 (2018) 803–824, https://doi.org/10.1007/s11242-018-1099-x.

[21] M.J. Skaug, L. Wang, Y. Ding, D.K. Schwartz, Hindered nanoparticle diffusion and void accessibility in a three-dimensional porous medium, ACS Nano 9 (2015) 2148–2159, https://doi.org/10.1021/acsnano.5b00019.

[22] K.H. Langley, I. Teraoka, 7. Light scattering and other optical methods, Exp. Methods Phys. Sci. 35 (1999) 263–300, https://doi.org/10.1016/S0076-695X(08)60418-4.

[23] L. Isa, CAPILLARY FLOW OF DENSE COLLOIDAL SUSPENSIONS, University of Edinburgh, 2007.

[24] Y. Liu, T. Yanagishima, A. Curran, K.V. Edmond, S. Sacanna, R.P.A. Dullens, Colloidal organosilica spheres for three-dimensional confocal microscopy, Langmuir 35 (2019) 7962–7969, https://doi.org/10.1021/acs.langmuir.9b00963.

[25] F. Della Sala, M. Biondi, D. Guarnieri, A. Borzacchiello, L. Ambrosio, L. Mayol, Mechanical behavior of bioactive poly(ethylene glycol) diacrylate matrices for biomedical application, J. Mech. Behav. Biomed. Mater. 110 (2020), 103885, https://doi.org/10.1016/j.jmbbm.2020.103885.

[26] F. Anjum, P.S. Lienemann, S. Metzger, J. Biernaskie, M.S. Kallos, M. Ehrbar, Enzyme responsive GAG-based natural-synthetic hybrid hydrogel for tunable growth factor delivery and stem cell differentiation, Biomaterials 87 (2016), https://doi.org/10.1016/j.biomaterials.2016.01.050.

[27] I. Strehin, Z. Nahas, K. Arora, T. Nguyen, J. Elisseeff, A versatile pH sensitive chondroitin sulfate-PEG tissue adhesive and hydrogel, Biomaterials 31 (2010) 2788–2797, https://doi.org/10.1016/j.biomaterials.2009.12.033.

[28] G.M. Pawar, M. Koenigs, Z. Fahimi, M. Cox, I.K. Voets, H.M. Wyss, R.P. Sijbesma, Injectable Hydrogels from Segmented PEG-Bisurea Copolymers, Biomacromolecules 13 (2012) 3966–3976, https://doi.org/10.1021/bm301242v.

[29] A.K. Gaharwar, C.P. Rivera, C.J. Wu, G. Schmidt, Transparent, elastomeric and tough hydrogels from poly(ethylene glycol) and silicate nanoparticles, Acta Biomater. 7 (2011) 4139–4148, https://doi.org/10.1016/j.actbio.2011.07.023.

[30] S. Ali, M.L. Cuchiara, J.L. West, Micropatterning of poly(ethylene glycol) diacrylate hydrogels, in: Methods Cell Biol, 1st ed., Elsevier Inc, 2014, pp. 105–119, https://doi.org/10.1016/B978-0-12-800281-0.00008-7.

[31] P. Debye, A.M. Bueche, Scattering by an inhomogeneous solid, J. Appl. Phys. 20 (1949) 518–525, https://doi.org/10.1063/1.1698419.

[32] F. Horkay, B. Hammouda, Small-angle neutron scattering from typical synthetic and biopolymer solutions, Colloid Polym. Sci. 286 (2008) 611–620, https://doi.org/10.1007/s00396-008-1849-3.

[33] S. Lee, X. Tong, F. Yang, Effects of the poly (ethylene glycol) hydrogel crosslinking mechanism on protein release, Biomater. Sci. 4 (2016) 405–411, https://doi.org/10.1039/C5BM00256G.

[34] C.-C. Lin, K.S. Anseth, PEG hydrogels for the controlled release of biomolecules in regenerative medicine, Pharm. Res. 26 (2009) 631–643, https://doi.org/10.1007/s11095-008-9801-2.

[35] W. Yang, H. Yu, W. Liang, Y. Wang, L. Liu, Rapid fabrication of hydrogel microstructures using UV-induced projection printing, Micromachines 6 (2015) 1903–1913.

[36] E.M. D'urso, G. Fortier, New bioartificial polymeric material: poly(ethylene glycol) cross-linked with albumin. I. Synthesis and swelling properties, J. Bioact. Compat. Polym. 9 (1994) 367–387, https://doi.org/10.1177/088391159400900402.

[37] M. Rossi, GELS BASED SYSTEMS FOR THE DEVELOPMENT OF FUNCTIONAL MATERIALS, University of Florence, 2019.

[38] F. Müller-Plathe, Different states of water in hydrogels? Macromolecules 31 (1998) 6721–6723, https://doi.org/10.1021/ma980685b.

[39] I.N. Savina, V.M. Gun'Ko, V.V. Turov, M. Dainiak, G.J. Phillips, I.Y. Galaev, S. V. Mikhalovsky, Porous structure and water state in cross-linked polymer and protein cryo-hydrogels, Soft Matter 7 (2011) 4276–4283, https://doi.org/10.1039/c0sm01304h.

[40] Z.H. Ping, Q.T. Nguyen, S.M. Chen, J.Q. Zhou, Y.D. Ding, States of water in different hydrophilic polymers - DSC and FTIR studies, Polym. (Guildf. ). 42 (2001) 8461–8467, https://doi.org/10.1016/S0032-3861(01)00358-5.

[41] T.N. Blanton, T.C. Huang, H. Toraya, C.R. Hubbard, S.B. Robie, D. Louër, H. E. Göbel, G. Will, R. Gilles, T. Raftery, JCPDS—International Centre for Diffraction Data round robin study of silver behenate. A possible low-angle X-ray diffraction calibration standard, Powder Diffr. 10 (1995) 91–95, https://doi.org/10.1017/S0885571590001441.

[42] F. Zhang, J. Ilavsky, G.G. Long, J.P.G. Quintana, A.J. Allen, P.R. Jemian, Glassy carbon as an absolute intensity calibration standard for small-angle scattering, Metall. Mater. Trans. A. 41 (2010) 1151–1158, https://doi.org/10.1007/s11661-009-9950-x.

[43] J.C. Crocker, D.G. Grier, Methods of digital video microscopy for colloidal studies, J. Colloid Interface Sci. 179 (1996) 298–310, https://doi.org/10.1006/jcis.1996.0217.

[44] D. Legland, I. Arganda-Carreras, P. Andrey, MorphoLibJ: Integrated library and plugins for mathematical morphology with ImageJ, Bioinformatics 32 (2016) 3532–3534, https://doi.org/10.1093/bioinformatics/btw413.

[45] D.B. Allan, T. Caswell, N.C. Keim, C.M. van der Wel, R.W. Verweij, soft-matter/trackpy: Trackpy v0.5.0. (2021). https://doi.org/10.5281/zenodo.4682814.

[46] E.I. Wisotzki, P. Tempesti, E. Fratini, S.G. Mayr, Influence of high energy electron irradiation on the network structure of gelatin hydrogels as investigated by small-angle X-ray scattering (SAXS), Phys. Chem. Chem. Phys. 19 (2017) 12064–12074, https://doi.org/10.1039/C7CP00195A.

[47] R. Mastrangelo, D. Chelazzi, G. Poggi, E. Fratini, L.P. Buemi, M.L. Petruzzellis, P. Baglioni, Twin-chain polymer hydrogels based on poly(vinyl alcohol) as new advanced tool for the cleaning of modern and contemporary art, Proc. Natl. Acad. Sci. U. S. A. 117 (2020) 7011–7020, https://doi.org/10.1073/pnas.1911811117.

[48] G. Shao, D.A.H. Hanaor, X. Shen, A. Gurlo, Freeze casting: from low-dimensional building blocks to aligned porous structures—a review of novel materials, methods, and applications, Adv. Mater. 32 (2020), https://doi.org/10.1002/adma.201907176.

[49] H. Nishihara, S.R. Mukai, D. Yamashita, H. Tamon, Ordered macroporous silica by ice templating, Chem. Mater. 17 (2005) 683–689, https://doi.org/10.1021/cm048725f.

[50] H. Shimizu, R. Wada, M. Okabe, Preparation and characterization of micrometer-sized Poly(N-isopropylacrylamide) hydrogel particles, Polym. J. 41 (2009) 771–777, https://doi.org/10.1295/polymj.PJ2009039.

[51] T. Moschakis, B.S. Murray, E. Dickinson, Particle tracking using confocal microscopy to probe the microrheology in a phase-separating emulsion containing nonadsorbing polysaccharide, Langmuir 22 (2006) 4710–4719, https://doi.org/10.1021/la0533258.

[52] V. Breedveld, D.J. Pine, Microrheology as a tool for high-throughput screening, J. Mater. Sci. 38 (2003) 4461–4470, https://doi.org/10.1023/A:1027321232318.

[53] E. Lushi, H. Wioland, R.E. Goldstein, Fluid flows created by swimming bacteria drive self-organization in confined suspensions, Proc. Natl. Acad. Sci. U. S. A. 111 (2014) 9733–9738, https://doi.org/10.1073/pnas.1405998111.

[54] F. Babayekhorasani, D.E. Dunstan, R. Krishnamoorti, J.C. Conrad, Nanoparticle diffusion in crowded and confined media, Soft Matter 12 (2016) 8407–8416, https://doi.org/10.1039/c6sm01543c.

[55] V.A. Dix, JA, Crowding effects on diffusion in solutions and cells, Annu. Rev. Biophys. 37 (2008) 246–263, https://doi.org/10.1146/annurev.biophys.37.032807.125824.

[56] F. Roosen-Runge, M. Hennig, F. Zhang, R.M.J. Jacobs, M. Sztucki, H. Schober, T. Seydel, F. Schreiber, Protein self-diffusion in crowded solutions, Proc. Natl. Acad. Sci. USA 108 (2011) 11815–11820, https://doi.org/10.1073/pnas.1107287108.

[57] L.M. Pappenheimer, J.R. Renkin, E.M. Borrero, Filtration, diffusion, and molecular sieving through porous cellulose membrane, Engl. J. 167 (1951) 13–46, https://doi.org/10.2307/801417.

[58] H. Brenner, L.J. Gaydos, The constrained brownian movement of spherical particles in cylindrical pores of comparable radius. Models of the diffusive and convective transport of solute molecules in membranes and porous media, J. Colloid Interface Sci. 58 (1977) 312–359, https://doi.org/10.1016/0021-9797(77)90147-3.

[59] J.M. Nitsche, G. Balgi, Hindered brownian diffusion of spherical solutes within circular cylindrical pores, Ind. Eng. Chem. Res. 33 (1994) 2242–2247, https://doi.org/10.1021/ie00033a030.

[60] G.M. Mavrovouniotis, H. Brenner, Hindered sedimentation, diffusion, and dispersion coefficients for brownian spheres in circular cylindrical pores, J. Colloid Interface Sci. 124 (1988) 269–283, https://doi.org/10.1016/0021-9797(88)90348-7.

[61] J.J.L. Higdon, G.P. Muldowney, Resistance functions for spherical particles, droplets and bubbles in cylindrical tubes, J. Fluid Mech. 298 (1995) 193–210, https://doi.org/10.1017/S0022112095003272.

[62] H. Happel, J. Brenner, Low Reynolds Number Hydrodynamics, with Special Applications to Particulate Media, in: Springer Sci. Bus. Media, 2012. https://doi.org/10.1007/bf00831902.

[63] Y. Pawar, J.L. Anderson, Hindered diffusion in slit pores: an analytical result, Ind. Eng. Chem. Res. 32 (1993) 743–746, https://doi.org/10.1021/ie00016a023.